PROCEEDINGS OF SPIE

Transition-edge sensor pixel parameter design of the microcalorimeter array for the x-ray integral field unit on Athena

Smith, S., Adams, J., Bandler, S., Betancourt-Martinez, G., Chervenak, J., et al.

SPIE.

Transition-edge sensor pixel parameter design of the microcalorimeter array for the X-ray Integral Field Unit on Athena

S. J. Smith*[a,b], J. S. Adams[a,b], S. R. Bandler[a], G. L. Betancourt-Martinez[a,c], J. A. Chervenak[a], M. P. Chiao[a,b], M. E. Eckart[a], F. M. Finkbeiner[d], R. L. Kelley[a], C. A. Kilbourne[a], A. R. Miniussi[e], F. S. Porter[a], J. S. Sadleir[a], K. Sakai[f], N. A. Wakeham[e], E. J. Wassell[g], W. Yoon[e], D. A. Bennett[h], W. B. Doriese[h], J. W. Fowler[h], G. C. Hilton[h], K. M. Morgan[h], C. G. Pappas[h], C. N. Reintsema[h], D. S. Swetz[h], J. N. Ullom[h], K. D. Irwin[i], H. Akamatsu[j], L. Gottardi[j], R. den Hartog[j], B. D. Jackson[k], J. van der Kuur[j], D. Barret[l], P. Peille[l].

[a]NASA Goddard Space Flight Center, Greenbelt, MD 20771, USA; [b]CRESST and University of Maryland, Baltimore County, MD 21250, USA; [c]University of Maryland, College Park, MD 20742, USA; [d]Wyle Information Systems Inc., McLean, VA 22102, USA; [e]NASA Postdoctoral Program, Universities Space Research Assoc., Greenbelt, MD 20771, USA; [f]CRESST and USRA, 7178 Columbia Gateway Drive, Columbia, Maryland 21046, USA; [g]Stinger-Ghaffarian Technologies, Greenbelt 20771, USA; [h]National Institute of Standards and Technology, Boulder, CO 80305, USA; [i]Stanford University, Palo Alto, CA 94305, USA; [j]SRON Netherlands Institute for Space Research, Sorbonnelaan 2, 3584 CA Utrecht, The Netherlands; [k]SRON Netherlands Institute for Space Research, Landleven 12, 9747 AD Groningen, The Netherlands; [l]IRAP, L'Institut de Recherche en Astrophysique et Planetologie, Toulouse, France

ABSTRACT

The focal plane of the X-ray integral field unit (X-IFU) for ESA's Athena X-ray observatory will consist of ~ 4000 transition edge sensor (TES) x-ray microcalorimeters optimized for the energy range of 0.2 to 12 keV. The instrument will provide unprecedented spectral resolution of ~ 2.5 eV at energies of up to 7 keV and will accommodate photon fluxes of 1 mCrab (90 cps) for point source observations. The baseline configuration is a uniform large pixel array (LPA) of 4.28" pixels that is read out using frequency domain multiplexing (FDM). However, an alternative configuration under study incorporates an 18 × 18 small pixel array (SPA) of 2" pixels in the central ~ 36" region. This hybrid array configuration could be designed to accommodate higher fluxes of up to 10 mCrab (900 cps) or alternately for improved spectral performance (< 1.5 eV) at low count-rates. In this paper we report on the TES pixel designs that are being optimized to meet these proposed LPA and SPA configurations. In particular we describe details of how important TES parameters are chosen to meet the specific mission criteria such as energy resolution, count-rate and quantum efficiency, and highlight performance trade-offs between designs. The basis of the pixel parameter selection is discussed in the context of existing TES arrays that are being developed for solar and x-ray astronomy applications. We describe the latest results on DC biased diagnostic arrays as well as large format kilo-pixel arrays and discuss the technical challenges associated with integrating different array types on to a single detector die.

Keywords: Imaging array, transition-edge sensor, x-ray spectroscopy

1. INTRODUCTION

The Advanced telescope for high-energy astrophysics (Athena) was selected as an L-class mission in ESA's 2015-2025 Cosmic Vision plan and has an anticipated launch date of 2028[1]. Athena is designed to address the science theme: 'The Hot and Energetic Universe', and as such will answer important questions related to the growth of black holes and large-scale structure in the Universe. Athena will have two instruments that can be interchanged at the focal-plane. The X-ray Integral Field Unit[2] (X-IFU), which is a cryogenic microcalorimeter array with a 5' field-of-view, and the Wide Field Imager[3] (WFI), which is a DEPFET active pixel sensor array with 40' field-of-view.

*stephen.j.smith@nasa.gov; phone 1-301-286-3719; fax 1-301-286-1684

The preferred technology for the X-IFU instrument is based around thin film superconducting transition-edge sensor (TES) thermistors that are operated in the sensitive transition region between the superconducting and normal states[4]. The detectors will be AC biased and read out using a frequency division multiplexer (FDM) based around superconducting quantum interference devices (SQUIDs)[5]. With revolutionary instrumentation, X-IFU will provide unprecedented high resolution imaging capabilities over the soft-x-ray energy band (0.2-12 keV), far beyond the capabilities of any existing observatory. In this paper we discuss the development of the TES detector arrays for X-IFU. We start by outlining the top level performance requirements and the proposed array configurations under study. These include a uniform array and a hybrid array of mixed pixel types. We present details of the device performance parameters that are being designed to meet the mission requirements and discuss the performance trade-offs between different detector designs. We also present latest results from uniform kilo-pixel arrays and smaller diagnostic arrays of mixed pixel geometries. Finally we discus the technical challenges associated with integrating arrays of different pixel types in to a single hybrid design.

2. X-IFU PERFORMANCE REQUIREMENTS AND ARRAY CONFIGURATIONS

2.1 Top level requirements and baseline array configuration

The preliminary performance requirements for the X-IFU are derived from the top-level science requirements[2] and are summarized in Table 1. The instrument will have a full-width-half-maximum (FWHM) energy resolution of $\Delta E_{\text{FWHM}} = 2.5$ eV at energies $E < 7$ keV and constant resolving power of $E/\Delta E = 2800$ for $E = 7\text{-}12$ keV. To significantly improve weak-line sensitivity, there is an improved resolution goal of $\Delta E = 1.5$ eV at energies below 1 keV. The array will accommodate photon fluxes of 1 mCrab (~ 90 cps) with 80% throughput for events graded as high-resolution ($\Delta E_{\text{FWHM}} < 2.5$ eV). There is an additional count-rate requirement at 1 Crab (~ 90000 cps) for the brightest source observations. However, this requires a throughput of 30% for low-resolution events only ($\Delta E_{\text{FWHM}} < 30$ eV). There is a further count-rate goal of 10 mCrab (~ 900 cps) with 80% high-resolution events, which will be important for studying bright gamma-ray burst afterglows and x-ray binaries. Finally, the quantum efficiency (including blocking filter transmission, absorber stopping power and fill factor) will be > 60 % at 1 keV and > 70% at 7 keV.

Table 1. Top-level requirements for the Athena X-IFU[2].

X-IFU Requirements	
Parameter	Requirement
Field of view	5'
Angular resolution	5"
Energy range	0.2-12 keV
Energy resolution (ΔE): E < 7 keV	2.5 eV (1.5 eV goal)
Resolving power ($E/\Delta E$): E > 7 keV	2800
Count-rate requirements:	1 mCrab (> 80% high resolution events)
	1 Crab (> 30% low resolution events)
Count-rate goal:	10 mCrab (> 80% high resolution events)
Quantum efficiency:	60% at 1 keV
	70% at 7 keV

As presently envisaged the baseline X-IFU configuration uses a sensor array of 3840 identical TES pixels in a single hexagonal array configuration. A hexagonal layout is preferred to better match to the cylindrical aperture in the magnetic shield design whilst enabling ease of tiling together composite observations[6]. With a telescope focal length of 12 m the equivalent diameter of the array will provide a field-of-view of 5' and a pixel pitch of 4.28" (249 μm). The point-spread-function (PSF) of the telescope optic has a half-power-diameter (HPD) of ~ 5". Figure 1 shows a schematic layout of the array configuration, commonly referred to as the uniform large pixel array (LPA). Also shown is the fraction of events absorbed in a subset of pixels for a point-source observation. For a 1 mCrab source the total flux corresponds to 87 cps with a maximum per pixel rate of 38 cps when the beam is centered on a single pixel (calculated by convolving 1 mCrab spectrum with the full instrument response[7], including the effective area of the telescope optics, the transmission of the blocking filter stack and the quantum efficiency of the detector, including the array fill-factor).
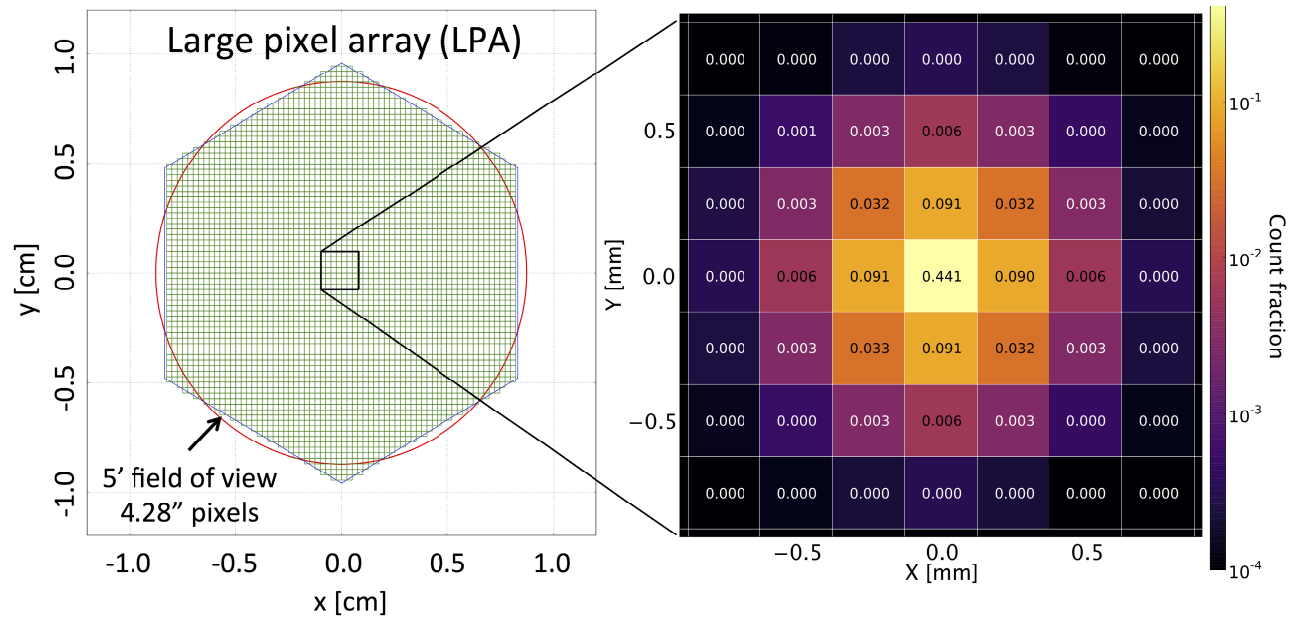
Figure 1. Uniform large pixel array (LPA) layout for the Athena X-IFU (left). The beam profile on the array assuming a 5" PSF is shown right. Depending upon the pointing accuracy and the use of dithering, slightly different per/pixel fraction can occur.

2.2 Hybrid Arrays

The baseline uniform LPA configuration is considered the simplest array to design and fabricate because all pixels are identical and based around a very well characterized concept. However, implementing this configuration for Athena means it will not be possible to achieve either the count-rate goal of 10 mCrab or the energy resolution goal of $\Delta E_{\text{FWHM}} =$ 1.5 eV. The use of identical pixels also represents an inefficient use of the read-out resources. This is because all pixels are optimized for the point-source count-rate requirement, even though, as depicted in Fig. 1, the 5" HPD of the PSF only spreads the beam over a relatively small region of the array (when centered on a single TES $\sim$ 44% of the events are on a single pixel). Using faster pixels over a larger extent of the array than is necessary requires significantly more system bandwidth and more dynamic range for the DAC's used for the baseband feedback and TES bias signals. Consequently, alternative options are also under consideration. For example, the project is examining the feasibility of including the ability to adjust the distance between the mirror assembly and the focal-plane (by $\sim$ 10's mm), thus defocusing the PSF, spreading the photons over a larger fraction of the array[2]. This would be targeted at achieving the 10 mCrab count-rate goal and the 1 Crab low resolution goal without having to re-design the focal-plane detectors. Alternatively, different parts of the focal-plane array could incorporate pixels optimized for different energy resolution, angular resolution or count-rate goals, whilst making more optimal use of the available readout resources. Such a hybrid array design could be optimized in a variety of ways to either significantly reduce the readout resources (and therefore the mass and power requirements of the X-IFU) necessary to meet the science requirements, or to provide science enhancements without requiring any additional resources than is already proposed. Although this approach is highly desirable, different pixel configurations are not as well verified as the standard design proposed for the uniform LPA and the ability to optimize different pixels independently when fabricated on a single detector die has not been fully demonstrated and introduces additional fabrication complexities. An example of a 'hybrid' design under study is shown in Fig. 2. This design incorporates an 18×18 small pixel array (SPA) of 2" pixels surrounded by a large-pixel array of 3476 pixels on a 4.50" pitch (262 μm). The SPA here would utilize faster TES designs with higher angular resolution and enable better imaging whilst accommodating the 10 mCrab (870 cps) goal for point source observations. The surrounding LPA pixels would only need to be optimized for extended source observations such as supernova remnants and galaxy clusters where the predicted maximum flux is $\sim$ 200 cps/arcmin^2. Such a hybrid array could in principle be optimized in different ways. For example, if defocusing the optics is a viable solution to achieve the 10 mCrab goal, an

SPA could then be optimized for the improved energy resolution goal $\Delta E_{\text{FWHM}} = 1.5$ eV at much reduced speed and dynamic range. It is worth noting that defocusing would be the only way to accommodate the 30% low-resolution throughput requirement at 1 Crab. In the next sections we examine the detector technology that is being developed for these different configurations.
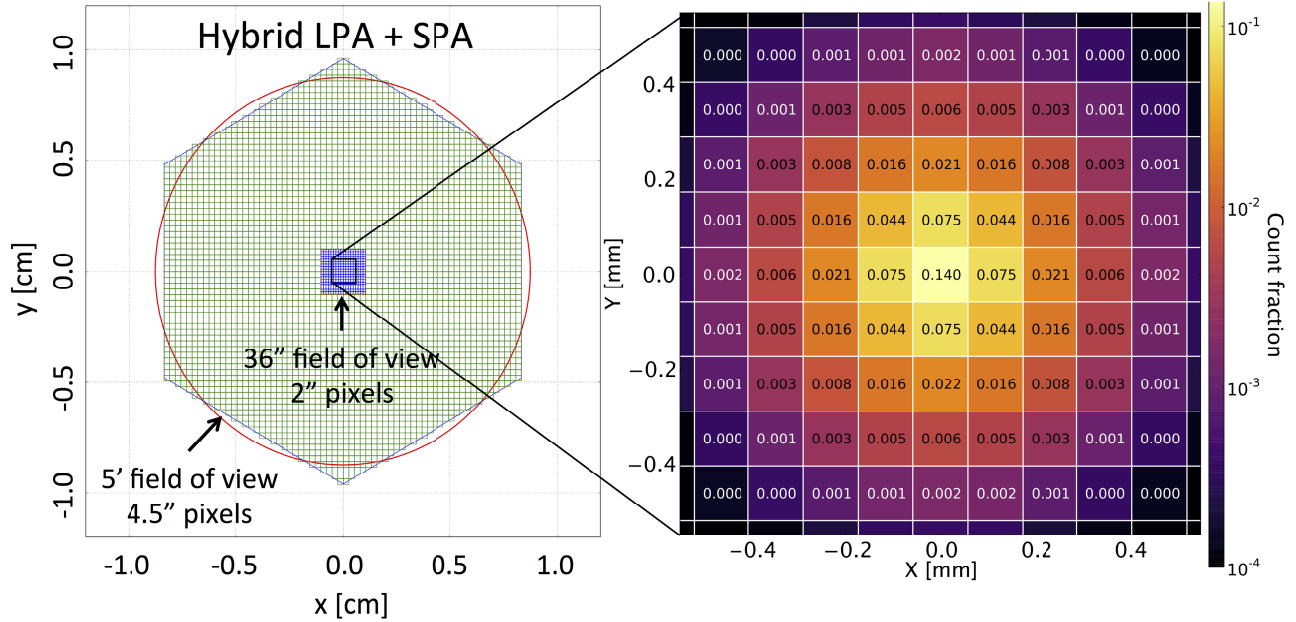

Figure 2. An example hybrid array that incorporates an 18×18 small pixel array (SPA) of 2" pixels optimized for 10 mCrab point-source observations and a large-pixel array of 4.50" pixels optimized for extended sources (~ few cps/pixel). The beam profile on the array assuming a 5" PSF is shown right.

2.3 Transition-edge sensor energy resolution and count-rate

The sensor array count-rate requirements significantly influence the choice of detector parameters and the optimal design of the readout architecture. For example, faster pixels can accommodate higher photon fluxes but require more readout bandwidth, DAC dynamic range for the bias and feedback signals and more SQUID dynamic range to keep flux excursions within tolerable limits[8]. Analysis of the optimal dimensioning the FDM readout chain is reported in van der Kuur et al. (2016)[9]. Here we evaluate the impact of the count-rate requirement on detector energy resolution. Photon arrival times are Poisson distributed events. The total time interval Δt required to process an x-ray event before another can be accepted determines the throughput for a given input flux. This must include both the record length, t_{rec}, required to analyze an event (using optimal filtering) and the time required for the previous event to have decayed to a negligible level, t_{rtb} ($\Delta t = t_{rec} + t_{rtb}$). For a given pixel, i with input rate of r_i, the fraction of events f_i accepted will be

$$f_i = e^{-r_i \Delta t}. \tag{1}$$

For high resolution events we require a net fraction of f = 80% summed across all pixels

$$f = \sum_i f_i = \sum_i \frac{r_i}{R} e^{-r_i \Delta t}, \tag{2}$$

where r_i/R is the ratio of the per pixel input rate to the total event rate (R = 1 mCrab). Equation 2 can then be solved to find Δt. For high resolution events the return to baseline time requires approximately 10 critically damped decay constants ($t_{\text{rtb}} = 10\ \tau_{\text{crit}}$) for the pulses to have decayed to a negligible level. The remainder of the time is allocated to the record length used for the event processing. The full-width-half-maximum energy resolution of a TES can be expressed in terms of its frequency dependent signal-to-noise ratio ($SNR(f)$)[4]:

$$\Delta E_{FWHM} = 2.355 \int_{df/2}^{\infty} \left(4\, SNR^2(f)\right)^{-1/2} df. \tag{3}$$

The width of each frequency bin is $df = 1/t_{rec}$. As discussed by Doriese et al. (2009)[10], in discretely sampled data the $f = 0$ bin has finite width and contains information about slow time varying offsets in the data stream as well as containing some of the measured x-ray signal information. The noise content usually suppresses the signal-to-noise ratio in that bin and can degrade the energy resolution. Thus, to appropriately evaluate ΔE_{FWHM} we integrate from the second frequency bin, $df/2$. In the limit of infinite record lengths $df \rightarrow 0$ and eq. 3 represents the best achievable energy resolution of the detector under the assumption of a linear energy scale and stationary noise sources. However, more generally t_{rec} is finite and is constrained by the specific count-rate requirements as described by eq. 2. Thus, the higher the count-rate requirements the shorter the record length and the greater the resolution degradation. The amount of degradation for a given pixel design is related to its effective information bandwidth, f_{eff}, and can be numerically evaluated from[10]:

$$f_{eff} = \frac{\int_0^\infty SNR^2(f) df}{SNR^2(0)}. \tag{4}$$

The resolution degradation for finite t_{rec} is then expressed as

$$\frac{\Delta E(t_{rec})}{\Delta E(t_{rec} \rightarrow \infty)} = (1 - 1/2 t_{rec} f_{eff})^{-0.5}. \tag{5}$$

The lower f_{eff} the more energy content will be lost to the $f = 0$ bin. Analytical evaluation of eq. 3, including only the two main sources of intrinsic detector noise (thermal fluctuation noise between the TES and the heat bath; $P_n = (4k_bT_0^2G_bF)^{1/2}$, and TES near-equilibrium Johnson noise; $V_n = (4k_bT_0R_0(1+2\beta))^{1/2}$) leads to the following expression for the small signal energy resolution[4],

$$\Delta E_{FWHM} \approx 2\sqrt{2\ln 2} \sqrt{\frac{4k_bT_0^2C}{\alpha} \sqrt{\frac{nF(T_0,T_b,n)(1+2\beta)(1+M^2)}{1-(T_0/T_b)^n}}}, \tag{6}$$

where C, T_0 and T_b are the device heat capacity, quiescent operating temperature and bath temperature respectively. The unit-less parameter $F(T_0,T_b,n) \sim 0.5$ accounts for the thermal gradient across the heat link to the bath and the constant n depends upon the physical nature of the thermal link. The resolution also depends upon the shape of the resistance transition $R(T,I)$, which is parameterized at the operating point by two unit-less partial derivatives $\alpha = T_0/R_0\ \partial R/\partial T$ and $\beta = I_0/R_0\ \partial R/\partial I$. The unexplained noise factor M^2 represents any additional noise sources intrinsic to the TES that are not explained by the TES Johnson noise alone. This is empirically determined from measured noise data.

The required instrument level resolution figure of 2.5 eV must accommodate not only the intrinsic energy resolution of the detector (including the effects of finite record length and detector non-linearity) but also additional noise terms from a variety of sources including the cold readout electronics, drifts due to variations in focal-plane assembly (FPA) environment, and noise generated by the cryo-harnessing and the warm front-end electronics. In order to appropriately accommodate the full (preliminary) error budget the detector should achieve < 2.0 eV (at 7 keV), and for events defined as high resolution, must be degraded by no more than 4% from the effects of finite record length. From eq. 5 this constrains the pixel bandwidth to $f_{eff} \geq 6.6/t_{rec}$. For events graded as mid-resolution (< 3 eV) and low resolution (< 30 eV) shorter record lengths are used to provide higher throughput at the expense of resolution. Detailed studies of the simulated performance with count-rate and energy, as well as studies of different pulse processing techniques, can be found in refs[11,12].
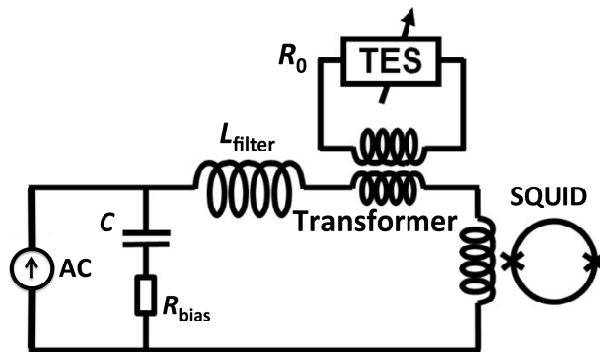

Figure 3. Schematic diagram of simplified bias circuit. The TES is transformer coupled to the main bias circuit. The effective inductance seen by the TES is $L_{eff} = L_{filter}/TTR^2$ and the effective load resistance, $R_{eff} = R_{bias}/TTR^2$. Further details on the readout architecture can be found in refs[6,9,18].

2.4 Baseline readout approach

TES arrays are conventionally read out using SQUID based multiplexers. The baseline readout approach for Athena uses 96-channel × 40-pixel frequency division multiplexing (FDM), that is being developed at SRON[5,13]. The low power SQUID amplifiers used in this system are developed at VTT (Finland)[14]. Alternative systems also under study use NIST/Stanford developed time/code division multiplexing (TDM/CDM)[15,16] of DC biased pixels. In the baseline FDM scheme the TESs are AC biased in a resonant LC circuit at frequencies in the range 1-5 MHz. Assuming ~ 40 TESs per multiplexed column these will be separated by ~ 100 kHz. The bandwidth of the LC filter depends on L and the resistance R of the sensor: $\Delta\omega = R/L$. The choice of $L = 2$ μH is driven by the desire to minimize the geometric size of the LC filter components[17]. The low operating resistances of the GSFC TESs ($R_0 \sim 1$ mΩ) necessitate transformer coupling to boost the effective sensor resistance by the square of the transformer turns ratio TTR^2. Figure 3 shows a schematic diagram of the AC bias circuit. In order to optimize system bandwidth the detectors are critically damped. In the transformer-coupled circuit the effective inductance seen by the TES is $L_{\text{eff}} = L_{\text{filter}}/TTR^2$, thus the TTR can be varied to critically damp the detector (typically TTR = 4-8). Any parasitic resistances or voltage biasing resistors ($R_{\text{bias}} \sim 1$ mΩ) in the circuit will also be transformed in to an effective load resistance, $R_{\text{eff}} = R_{\text{bias}}/TTR^2$. Note that R_{eff} has an analogous physical interpretation to the voltage biasing shunt resistor used in the DC bias circuit, contributing electrical Johnson noise and reducing electro-thermal feedback. The effective critical damping inductance L_{crit} as seen by the TES depends on the circuit and TES parameters

$$L_{crit} = k \frac{R_0 \tau_0}{(L_I - 1)^2} \left[L_I \left(3 + \beta - \frac{R_{eff}}{R_0} \right) + \left(1 + \beta + \frac{R_{eff}}{R_0} \right) - 2 \sqrt{L_I (2 + \beta) \left(L_I \left(1 - \frac{R_{eff}}{R_0} \right) + 1 + \beta + \frac{R_{eff}}{R_0} \right)} \right]. \tag{7}$$

Here $\tau_0 = C/G_b$ is the natural decay constant and $L_I = \alpha P_0/T_0/G_b$ is the loop gain of the electro-thermal feedback. Since L_{crit} depends on R_{eff} (which is scaled by TTR) and TTR also depends on L_{crit}, eq. 7 is numerically solved to simultaneously find the self-consistent values of L_{crit}, TTR and R_{eff}. Note that the equivalent inductance required to critically damp the detector in FDM ($k = 1/2$) is half that for TDM/CDM ($k = 1$). Finally the electro-thermal decay constant of the detector is given by:

$$\tau_{etf} = \frac{\tau_0}{1 + L_I \frac{1 - R_{eff}/R_0}{1 + R_{eff}/R_0 + \beta}}. \tag{8}$$

In the limit of low inductance ($L \ll L_{\text{crit}}$) this is equivalent to the fall time of the x-ray pulses, however, when $L \approx L_{\text{crit}}$ the critically damped time constant of the detector τ_{crit} will be faster by a factor of around 2-4 depending on the specific detector parameters.

Table 1 shows a summary of the key detector parameters and performance metrics for the uniform LPA and an example Hybrid LPA+SPA detector. The details of the pixel designs are discussed in the following sections.

Table 1. Proposed pixel parameters and performance metrics for the current baseline uniform large pixel array and a hybrid array consisting of both a large and small pixel array. The description of the TES parameters is discussed in the main text. Also shown is the $\Delta E_{\text{FWHM}}(t_{\text{rec}})$ calculated for infinite record length and for calculated finite record length required accommodate the specified count-rate. The calculation assumes the flux distributions shown in Figs. 1 and 2. All pixel parameters assume $T_0 = 90$ mK and $T_b = 55$ mK. The max. dI/dt is the calculated maximum current slew-rate in the TES from an x-ray event. The maximum count-rate accommodation to keep the energy resolution degradation to the 4% allocation in the error budget is also shown. The proposed SPA pixel has very similar resolution to the LPA pixels but the critically damped time constant is twice as fast and the information bandwidth is twice as large. The ability to accommodate the 10 mCrab goal is mainly achieved by oversampling the PSF.

Detector parameters			
Parameter	Uniform LPA	Hybrid LPA	Hybrid SPA
Pixel size	249 μm	262 μm	115.5 μm
G_b	200 pW/K	115 pW/K	300 pW/K
C	0.8 pJ/K	0.8 pJ/K	0.26 pJ/K
α	75	75	100
β	1.25	1.25	10
M^2	0	0	0.8
R_0	1 mΩ	1 mΩ	1.1 mΩ
I_0	68.1 μA	51.5 μA	72.6 μA
$P_0 = I_0^2 R_0$	4.63 pW	2.65 pW	5.8 pW
TTR	5.47	4.08	4.01
R_{eff}	33 μΩ	60 μΩ	62 μΩ
L_{eff}	67 nH	121 nH	124 nH
τ_{etf}	436 μs	788 μs	306 μs
τ_{crit}	160 μs	286 μs	79 μs
f_{eff}	963 Hz	553 Hz	1714 Hz
Max. dI/dt	85 mA/s/keV	36 mA/s/keV	220 mA/s/keV
Count-rate	1 mCrab	200 cps/arcmin^2	10 mCrab
Δt	12 ms	200 ms	5.1 ms
$t_{\text{rec}} = \Delta t - 10\tau_{\text{crit}}$	10.4 ms	197 ms	4.3 ms
$\Delta E_{\text{FWHM}}(\infty\ t_{\text{rec}})$	1.70 eV	1.71 eV	1.55 eV
$\Delta E_{\text{FWHM}}(t_{\text{rec}})$	1.75 eV	1.71 eV	1.60 eV
Max. count-rate 4% degradation	1.4 mCrab	2.7 kcps/arcmin^2	10 mCrab

3. ARRAY DESIGN AND TECHNOLOGY DEVELOPEMENT

3.1 Large pixel array design

The preferred array technology for the X-IFU is based around thin-film transition-edge sensors developed at NASA Goddard Space Flight Center[19-20]. This array technology has previously been developed for various other proposed x-ray observatories such Constellation-X and the International X-ray Observatory (IXO)[21]. The top-level science requirements and array performance metrics are very similar. The parameters listed in Table 1 for the LPA reference pixel were originally based on the measured parameters of a series of uniform 8 × 8 arrays made at GSFC[22] and identical to that proposed for IXO (other than a slightly reduced pixel pitch from 300 μm for IXO). The TES device design (see Fig. 4) consists of a 140 μm-square Mo/Au bilayer deposited atop a silicon-nitride membrane (typically 0.5-1 μm thick) to form a thermal link to the heat sink at temperature $T_b \sim 55$ mK, and an x-ray absorber provides stopping power for the x-rays. Thick banks of Au are deposited along the edges parallel to the current flow to define the superconducting boundary condition and interdigitated gold stripes are oriented perpendicularly to the current flow, which has been shown to reduce the unexplained white noise associated with TES devices.
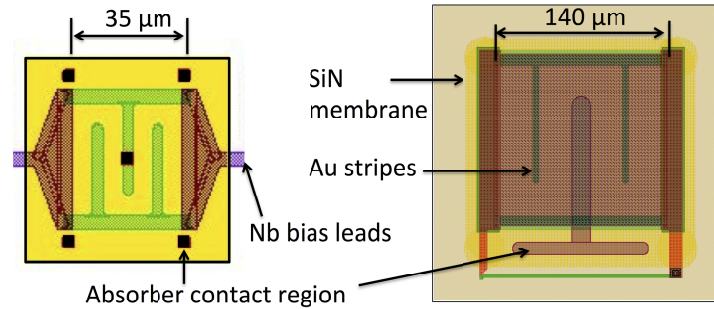
Figure 4. Schematic diagram of two different TES pixel geometries. Shown is a small TES design (left) that is considered for the SPA pixels and larger pixel design (right) proposed for the LPA. The two images are not to relative scale.

The Mo/Au bilayer has a resistance of ~ 15 m$\Omega/\square$ This is reduced by the normal metal features atop the TES such that the normal state resistance, $R_n \approx 8\text{-}10$ mΩ. At typical bias points in the transition of 1-2 mΩ the small signal transition parameter, α, ranges from 50-150, and β, ranges from 1-2. The measured noise is generally consistent with Irwin's prediction of non-ohmic Johnson noise near equilibrium[4], thus $M^2 \approx 0$. Micro-striped Nb electrical bias leads, deposited on a 4 μm pitch, provide the high density wiring between pixels that is necessary to fully wire out kilo-pixel arrays. A Cu layer (> 2 μm thick) is deposited on the backside of the Si chip and up the sidewall of the Si muntin (silicon mesh between pixels after the membrane defining deep reactive ion etching of the Si below TESs). This is to provide adequate heat-sinking of the interior of the array to the heat-bath and to reduce thermal cross-talk between pixels[23]. The absorbers are cantilevered over the TES and membrane, making contact in a T-shaped region that provides the thermal connection to the TES. Success with the T-shaped absorber contact led to their incorporation into GSFC uniform arrays and the presumed configuration of the reference design. However different geometric absorber contact regions have been shown to modify the pixel transition properties and future geometric optimizations cannot be ruled out[24]. Figure 5 shows an optical micrograph of a prototype 32×32 array of uniform pixels. These arrays are fully wired within the interior of the array and 64 pixels are connected to bond pads on each side of the array (in total, a quarter of all TESs). This type of array will be used for initial X-IFU technology demonstrations for both FDM readout and TDM/CDM readout. Also shown in Fig. 5 is a combined spectrum for 500×10^3 counts from 26 pixels measured at Al-Kα (1.5 keV), read out using a TDM system (similar to that described in Doriese et al. (2016)[15]). The array used for these measurements exhibited some non-ideal characteristics, including lower than targeted T_C (~ 82 mK) and a larger than standard T_C gradient across the array (detailed properties of this array are discussed in Smith et al. (2015)[25]). Despite this the RMS resolution of the 26 pixels was $\langle \Delta E_{\text{FWHM}} \rangle = 2.31 \pm 0.1$ eV consistent with the fitted result for the combined spectrum shown in Fig. 5. Similar measurements at Mn-Kα (5.9 keV) on 26 pixels achieved $\langle \Delta E_{\text{FWHM}} \rangle = 2.95 \pm 0.14$ eV. This is slightly worse because of non-linearity in the detector response and T_C non-uniformity across the array (and is not related to the performance of the TDM readout system). This was exacerbated by a larger than typical magnetic field gradient across the array during this particular measurement. Given an array with suitable characteristics and recently improved magnetic shielding we should expect to achieve $\langle \Delta E_{\text{FWHM}} \rangle < 2.5$ eV. The first kilo-pixel arrays will be tested with FDM read-out at SRON in the near future.
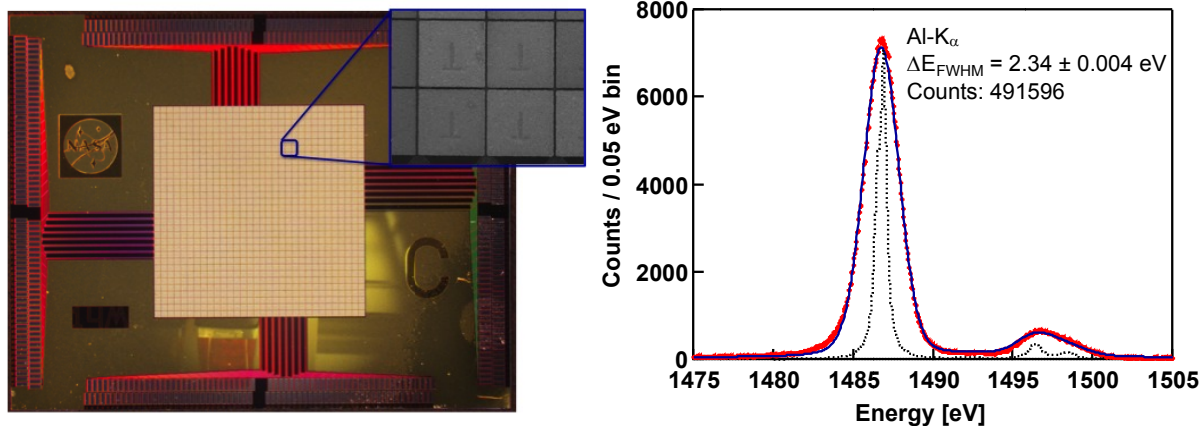
Figure 5. Left) Photograph of a 32×32 array of Mo/Au TES with Au/Bi absorbers on a 250 μm pitch. The inset shows an SEM image of the absorbers. Right) Combined spectrum from 26 pixels in 32 × 32 array readout using a time-division-multiplexer (TDM) system. This particular array had $T_0 \approx 82$ mK, $C \approx 0.6$ pJ/K, $G_b \approx 170$ pW/K, $R_n \approx 6$ mΩ and $\tau_{crit} \approx 280$ μs.

Due the nature of the voltage biasing circuit and the shape of the resistive transition, TES detectors are intrinsically non-linear devices. The initial temperature rise when an x-ray event is absorbed is $\Delta T = E/C$. If ΔT is too large, the change in TES current and resistance may be highly non-linear. Since C also impacts the noise (eq. 6) there is a trade-off between the small signal resolution and the linearity at larger energies. The target C is therefore chosen to achieve a quasi-linear response up to energy range of interest. In our Athena LPA designs we are targeting < 20% resolution degradation due to non-linearity at energies up to 7 keV. Our arrays use electroplated Au or more typically composite Au/Bi absorbers[26]. The Au layer provides rapid thermal diffusion to the TES at the expense of a high electronic specific heat capacity. An additional layer of the semi-metal Bi provides increased stopping power for x-rays but due to its low electron density, (~ 10^{17} cm^{-3}, as opposed to ~ 10^{22} cm^{-3} for a normal metal) the heat capacity contribution from the electronic component is much smaller than for a metal and is in fact comparable to the lattice component at mK temperatures[27]. Depending upon the desired pitch the relative thickness of the Au/Bi can be adjusted to achieve the target heat capacity whilst maintaining the required quantum efficiency. The TES bilayer and the SiN membrane are also expected to contribute small amounts to the total heat capacity. To achieve the proposed instrument requirement of > 70% QE at 7 keV, the baseline LPA absorbers require a vertical QE of > 90%. The targeted QE and total heat capacity target of $C \approx 0.8$ pJ/K at 90 mK can be simultaneously achieved using a 1.7 μm Au / 4.2 μm Bi composite absorber. Figure 6 shows the vertical QE as well as the total QE assuming an areal fill-factor of 96.8% (achieved with a 4 μm gap between pixels). Table 2 summarizes the estimated contribution of each component to the total device heat capacity.

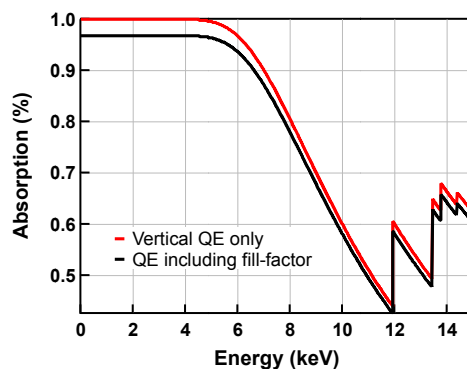Figure 6. Calculated absorber QE for the baseline LPA assuming 1.7 μm Au / 4.2 μm Bi absorbers. Shown are both the vertical QE and the total QE assuming 96.8 % fill factor that can be achieved with 4 μm gaps between pixels.

Table 2. Calculated heat capacity budget for the proposed baseline LPA pixels, assuming 1.7 μm Au / 4.2 μm Bi thick absorbers that will provide a vertical QE of 90% at 7 keV. The SiN heat capacity value is the measured value from Eckart et al. (2009)[28] and the Bi value is calculated from Collan et al. (1970)[27].

Heat Capacity Budget		
Component	Contribution	% of Total
Absorber Au:	0.64 pJ/K	80 %
Absorber Bi:	0.02 pJ/K	3 %
TES:	0.09 pJ/K	11 %
SiN membrane:	0.05 pJ/K	6 %
Total:	**0.8 pJ/K**	**100 %**

The thermal conductance to the heat bath is determined by the quasi-ballistic phonon transport in the SiN membrane[29] and is sensitive to its thickness, d as well as the surface roughness. For a given d, G_b will scale with the phonon-emitting perimeter of the TES in contact with the SiN and exhibits an exponent of the temperature dependence equivalent to $n \approx 3$ ($G_b \propto T^{n-1}$). To accommodate the 1 mCrab count-rate requirement for the uniform LPA the target thermal conductance is nominally 200 pW/K. This results in a ~ 3% degradation in resolution, slightly less than the target value. This is a little lower than the present design which has G_b ~ 275 pW/K at 90 mK. If an SPA in a hybrid configuration were used to accommodate higher fluxes, the requirements for the LPA could be significantly reduced. The count-rate requirement is then driven by extended sources where the predicted flux is ~ 200 cps/arcmin^2 (equivalent to ~ 1 cps/pixel). Analysis of the required readout resources for the uniform and hybrid configuration suggest that a reduction in G_b for the hybrid LPA of a factor of ~ 2, coupled with using the faster pixels in the SPA would require similar readout resources compared to the uniform LPA. A reduction by a factor of 4 in G_b for the hybrid LPA would enable a significant reduction in required resources (~ 60%). Thus we are exploring reduced G_b options in the range (30-115 pW/K) for a hybrid LPA. Note that the proposed reduction in G_b (< 115 pW/K) is based around what may be practically feasible to fabricate and is not scaled to be commensurate with the reduced count-rate requirements. Since the record lengths can be very long compared to the decay time constant the calculated ΔE_{FWHM} for high resolution events shows no degradation. Thus there is significant margin in these pixels to accommodate greater rates (~ 15 cps/pixel) with shorter t_{rec} and still achieve 4% resolution degradation. However this additional margin may also be beneficial as it allows for larger noise terms in the full error budget analysis. Although the proposed parameter sets are identical except for the reduced G_b, in reality changes in pixel geometry and G_b have the potential to impact the detector transition properties (α, β, M^2). For example, adjustments to pixel design will affect self-induced magnetic fields from current flowing in the sensor and electric bias contacts, as well as the complex interplay between non-equilibrium superconductivity effects and proximity effects from electrical bias leads and the noise mitigation features[30,31,32]. In combination, these effects are very difficult to predict even for small perturbations in design around the well-established reference. We have recently begun an experimental campaign to examine the impact on detector parameters resulting from such design perturbations. These include:

1. Variations in TES size. Recent thermal conductance measurements on TESs with lateral size in the range $L =$ 100-140 μm showed G_b(90 mK) ≈ 275 pW/K × (L / 140 μm). Thus a 100 μm TES is close to the target G_b for the uniform LPA. We are also exploring the option of reducing the TES size to ~ 50 μm which should reduce G_b even further.

2. Reduced SiN thickness. In the 2-dimensional limit G_b is expected to scale with d. Recent designs use $d = 1$ μm, however we have historically used $d = 0.5$ μm with similar detector designs and achieved $G_b \approx 160$ pW/K at 90 mK[20]. We have already switched back to 0.5 μm SiN on the newest diagnostic wafers (though they are provided by a different vendor) for thermal characterization.

3. Front etch perforations. By slotting the SiN around the pixel the phonon-emitting perimeter and therefore G_b is reduced. Previously tested devices with perforations in the range 25 - 75% show good consistent scaling of G_b with perforation fraction. Recent tests on 32×32 arrays with perforated membranes showed non-ideal transition characteristics and distorted critical current measurements. We are studying whether this is due to changes in the membrane stress affecting the bilayer properties, or a fabrication issue related to the added processing steps.

3.2 Recent experimental results

In order the better understand the impact of device geometry on TES performance we have recently characterized devices of sizes 100, 120 and 140 μm in 8×8 test arrays. These devices have Au(1.35 μm)/ Bi(3.0 μm) thick absorbers and a measured heat capacity of $C \approx 0.68$ pJ/K at $T_0 \approx 92$ mK. Figure 7 shows the R vs T derived from measured current-voltage curves at $T_b \approx 55$ mK. Also shown is the unit-less derivative of these R-T curves, α_{IV}. The shapes of the transitions are generally quite similar, though there are systematic differences in R_n and T_C. This is attributed to the role of the normal metal features atop the TES, which proximitizes the surrounding area and suppresses T_C. These features also act as low resistance parallel current paths that reduce R_n[30]. These features cover a larger fraction of the TES area for the smaller pixel size, meaning the impact on the transition is greater. We measured an average pixel resolution of $<\Delta E_{FWHM}> = 2.22 \pm 0.15$ eV for 13 pixels (7× 140 μm, 4× 120 μm, 2× 100 μm) for Mn-Kα x-rays (5.9 keV). There was no statistically significant difference in resolution between the pixels of different sizes at operating points of ~15-25% R_n. For comparison the measured baseline resolution ΔE_{BL} derived from histograms of randomly triggered noise events shows $<\Delta E_{BL}> = 1.93 \pm 0.14$ eV. Although the spectral performance at 6 keV is well characterized and quite linear, the higher energy response is less understood and depends on a detailed understanding of the large-scale transition shape and noise properties.

We have thus begun a campaign to characterize energies up to 12 keV (the upper energy range for X-IFU). Figure 8 shows the resolution as a function of energy for a single 100 μm device operating at a bias point of ~ 15% R_n. Also shown is the Cu-Kα (8.05 keV) and Br-Kα (11.9 keV) spectral fits for the same pixel. These line complexes were generated using a secondary fluorescence x-ray source with Mn, Cu and Br targets. Note that the Au L_{IIII} absorption edge (11.92 keV) straddles the Kα1 and Kα2 lines in the Br complex (as illustrated in Fig. 6), thus the fitted line shape was re-normalized to account for the calculated difference in absorber QE on either side of this absorption feature (51% above and 36% below). This device showed excellent spectral performance up to 12 keV. To provide context the dotted line in Fig. 8 shows X-IFU instrument resolution, though we note that direct comparison is not straightforward since laboratory measurements include some broadening terms that may be different to the full X-IFU error budget. Also shown in Fig. 8(d) is the optimally filtered energy as a function of the known energy from different fluorescent targets. The curvature in the gain scale is ~1.8× steeper at the origin than at 13 keV. Measurements on a 140 μm pixel showed very similar spectral performance at Mn-Kα and Cu-Kα, though slightly worse at Br-Kα, $\Delta E_{FWHM} = 4.2 \pm 0.16$ eV. We estimate that a 12 keV x-ray event will transverse from the 15% R_n operating point to ~ 50% R_n (equivalent to ~ 4.7 mΩ) thus sampling a significant fraction of the transition. Although the measured transition shapes are quite similar between designs there are subtle differences in fine structure between them that may impact the resolution performance at higher energies. Further x-ray measurements are required at different bias points to better understand the linearity difference between the different geometries.
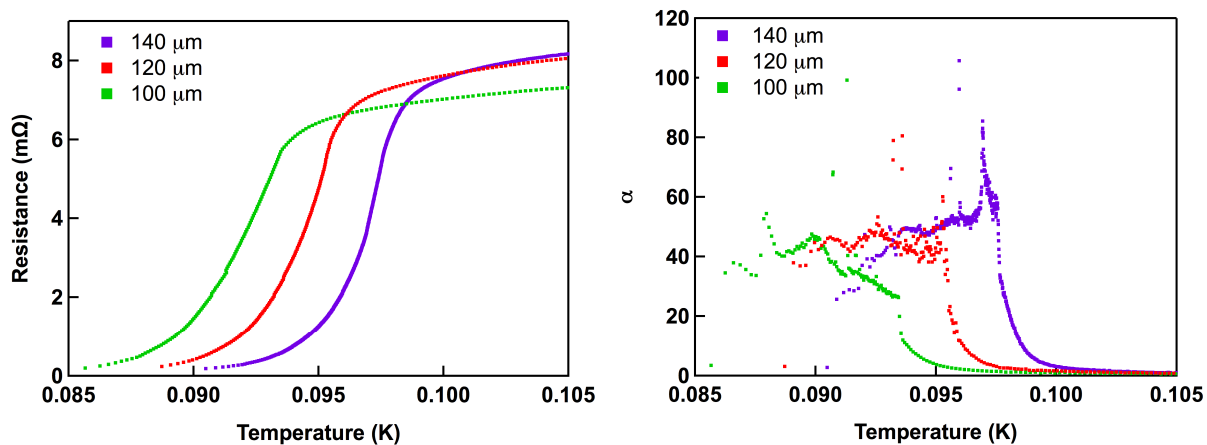

Figure 7. Left) Measured R vs T curves for 3 devices of different sizes. The data are derived using the measured thermal properties of the TES and measured current-voltage (IV) curves at $T_b \approx 55$ mK. Right) Composite α_{IV} derived from the R-T curves shown left. Note that this differs from the definition of α at constant current since both current and temperature are changing through the measured IV curve (approximately, $\alpha_{IV} \approx \alpha/(1+\beta/2)$).
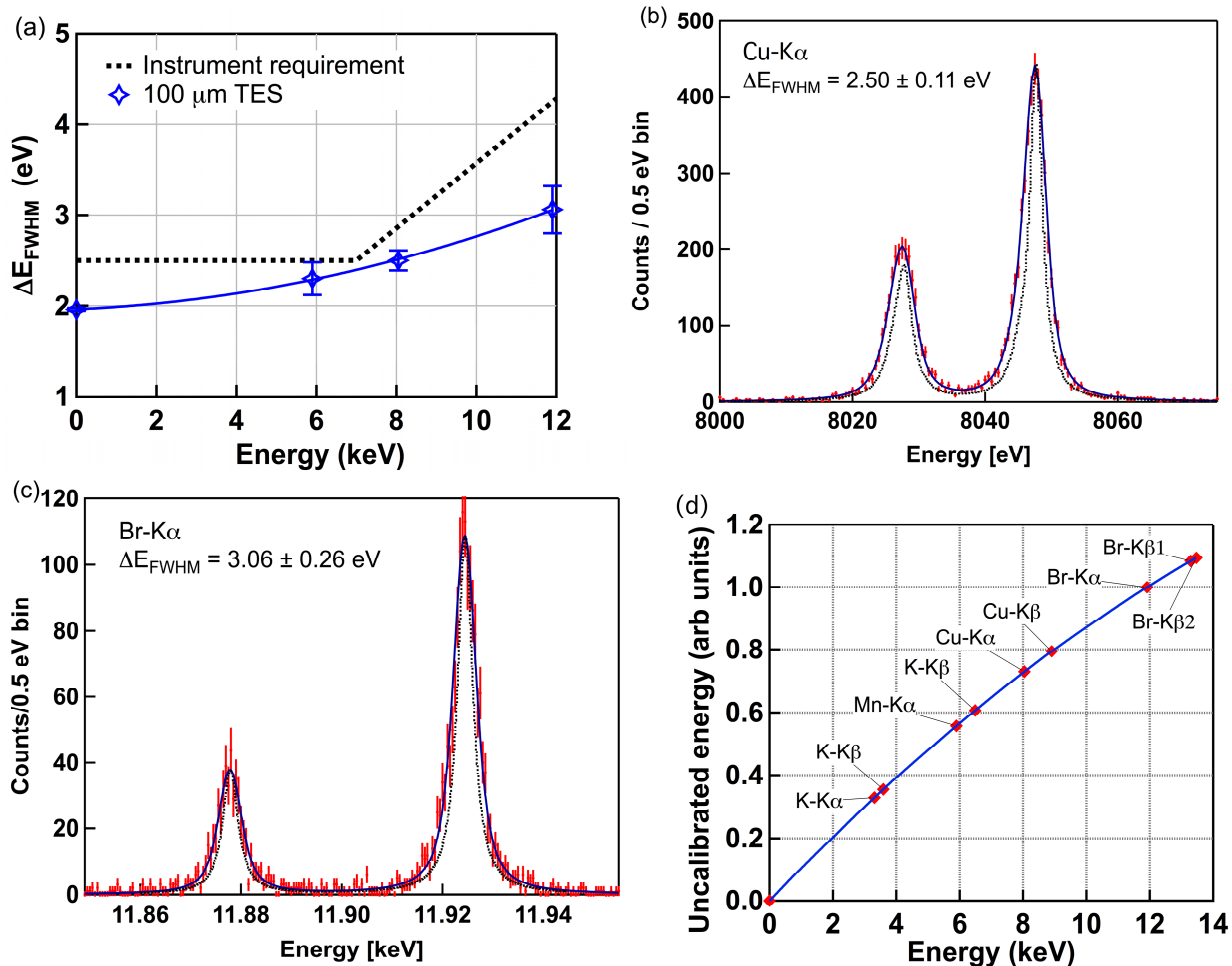
Figure 8. (a) Measured ΔE_{FWHM} as a function of energy for a 100 μm device. The blue line is a polynomial fit to the data. Shown in (b) and (c) are the Cu-Kα (8.05 keV) and Br-Kα (11.9 keV) spectral fits for the same pixel. The dashed line shows the intrinsic line shapes derived from refs[33,34,35]. The solid lines are the best fit to the data assuming a Gaussian instrument response. Also shown (d) is the optimally filtered energy as a function of the known energy from different fluorescent targets indicated on the figure. The curvature in the gain scale is indicative of the detector non-linearity and is ~1.8× steeper at the origin than at 13 keV.

We are also carrying out systematic studies of gain sensitivities to perturbations in T_b and magnetic field, B in order to better constrain the susceptibility of the device performance to variations in the focal-plane assembly environment. In laboratory measurements variations in gain of the order 1% over long time scales (> minutes) can be removed by gain correction algorithms with no significant degradation in resolution. However, variations over shorter, pulse-to-pulse time scales that cannot be accurately tracked have the potential to degrade resolution and must be included in the instrument error budget. The shape of a resistive transition is a function of temperature, current and magnetic field $R(T,I,B)$ and is closely related to the field and temperature dependence of the critical current $I_C(T,B)$. The proximity effects from the interaction between the different superconducting/normal materials results in a Fraunhofer-like modulation of the critical current with applied magnetic field[31]. The total magnetic field seen by the TES includes any externally applied fields as well as self-induced fields from current flowing in the TES and biasing leads. The period of this modulation is equivalent to one magnetic flux quantum penetrating the film. The flux penetrating the sensor is given by, $\Phi = B/A_{eff}$, where A_{eff} is the effective area of the TES that is sensitive to the field. Detailed measurements of the $I_C(T,B)$ and transition parameters on a single 140 μm have previously been reported in Smith et al.[36]. Measurements of the periodicity of the $I_C(B)$ for the devices reported here confirm a linear scaling with TES area. Reducing the size from 140 μm to 100 μm, reduced A_{eff} by a factor of ~ 2 and a larger B is required to achieve the same Φ. Thus, it is possible

smaller pixels may be less sensitive to time varying drifts in the magnetic field environment or static magnetic field gradients over the array. In order to study the impact of magnetic field on gain sensitivity we have measured the pulse shape as a function of bias point and magnetic field. Figure 9 shows the measured pulse height for Mn-Kα x-rays as a function of applied magnetic field for each device. The points labeled 'A' through 'F' correspond to a subset of points where high-resolution spectra were obtained. The oscillatory behavior reflects the changes in $I_C(B)$ which in turn change the α and β and hence the pulse shape. Variations in the optimally filtered energy are tracked for small perturbations in applied field, dE/dB. The largest dE/dB occurs where the pulse shape changes the most with applied B. For example at point 'A', dE/dB = 1.75 eV/nT whereas at point 'B', dE/dB = -0.1 eV/nT, more than an order of magnitude lower. Although the oscillation period is increased for the smaller devices, the fractional changes in the pulse heights are in general larger. Thus, depending upon the applied B, the smaller devices can have larger dE/dB. Since the bias path across the $R(T,I,B)$ surface is determined by the equilibrium power balance between the joule heating in the sensor and the heat flow to the heat bath, the exact manifestation of these features will vary depending upon G_b and T, and is very difficult to predict a priori.

Measurements of dE/dT_b have also been carried out. Fluctuations in T_b change the equilibrium bias point resistance of the TES and change the apparent energy. Thus dE/dT_b is not generally correlated with dE/dB. We measured an average of dE/dT_b = -48.5 ± 0.24 meV/μK for 7 measurements. The values for the subset of points shown in Fig. 9 are listed in the caption. The achievable static magnetic field environment for the Athena FPA will be ~ 1 μT with array scale uniformity of ~ 0.1 μT[6]. This should be sufficient to achieve a high degree of performance uniformity over the whole array. Since a magnetic field coil will be used to cancel any static stray fields, a larger offset could be used to bias the detectors in a less magnetically sensitive part of the $R(T,I,B)$ phase space. Detailed comparisons with TES detector models will be carried out in the near future. This will be important to better understand how the different detector designs, with different transition parameters, affect the gain sensitivities.
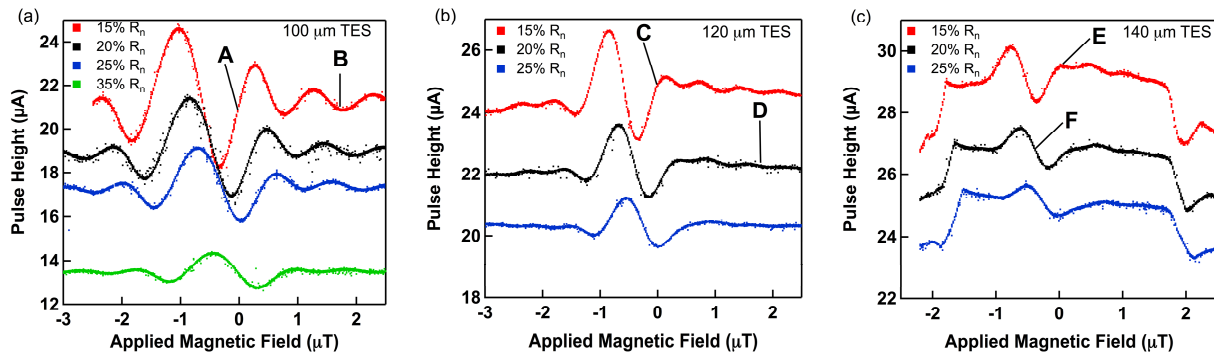

Figure 9. Measured Mn-Kα pulse height versus applied magnetic field and bias point resistance for a 100 μm (a), 120 μm (b) and 140 μm (c) device. The energy gain sensitivity dE/dB at the points labeled A-F are 1.75, -0.1, 0.33, -0.06, 0.05 and -0.6 eV/nT respectively. Similar measurements of the energy gain sensitivity to fluctuations in bath temperature dE/dT_b at the same points are -100, -47, -44, not measured, -27, -40 meV/μK respectively.

The Mo/Au TESs under study for Athena were originally designed and developed for DC biased schemes read out with TDM/CDM. Studies of a uniform GSFC 8×8 array under AC bias at SRON had previously shown different transition characteristics and have not yet converged on the same resolution performance seen under DC biased pixels[37]. Efforts to understand the differences have focused around understanding how the AC bias affects the transition shape differently to DC biased pixels and how the AC magnetic field couples to metal features in the pixel design (absorber, metal stripes). The 8×8 test array discussed above (of mixed pixel geometries) is presently in testing at SRON. We have recently demonstrated improved performance of $\Delta E_{FWHM} \approx 2.5$ eV at Mn-Kα on a 120 μm device with a measured noise level equivalent to 2.0 eV (estimated from eq. 3 using the measured $SNR(f)$). The details of this and the status of the FDM development are reported in Akamatsu et al. (2016)[18]. Additional devices with geometric variations specifically targeted at studying AC performance have now been designed and will be tested soon. We now have AC bias test set-ups at both GSFC and NIST for supporting pixel characterization studies.

3.3 Small pixel array development

The SPA parameters listed in Table 1 are based on a pixel design originally developed for solar physics applications[38]. A schematic diagram of the pixel is shown in Fig 4. This particular pixel design is often referred to as a high dynamic range, high count-rate option because of the excellent spectral resolution and count-rate capability demonstrated over a wide range of energies. This particular device had a signal decay time of $\tau_{\text{etf}} = 200$ μs, and was able to accommodate relatively high count rates of above 100 counts per second without significant energy resolution degradation[39]. Figure 10 shows the measured spectral resolution as a function of energy (up to Cu-Kα) as well as the measured Mn-Kα spectrum.

The basic pixel design consists of 35 × 35 μm Mo/Au TESs with all Au absorbers 4.5 μm thick and with lateral dimensions of 64 × 64 μm². In the original design no bismuth layer is required because the heat capacity of small pixel sizes is sufficiently small to provide the required properties (e.g. ΔE and QE) using Au alone. Scaling these pixels to the significantly larger pixel pitch proposed for the SPA (115.5 μm) with the same absorber thickness would introduce too much total C. Thus in order to meet the resolution and count rate requirement we are aiming for $C = 0.26$ pJ/K, which is approximately 2 times higher than the original pixel designs that they were based on. Since the small signal energy resolution scales with $\sqrt{C}$, the predicted SPA resolution is now 1.6 eV. To achieve the QE requirement a composite Au(3.25 μm)/Bi(1.5 μm) would be required, alternatively a slightly reduced QE requirement would enable all Au. In order to achieve a sufficiently high G_b, required for high count-rate capability, these pixels lack the membrane-defining back-etch of the LPA design. The thermal conductance to the heat-bath is then determined by the Kapitza-coupling at the interface between the TES bilayer and the substrate ($G_b \propto T^3$, $n = 4$) rather than the properties of the membrane. These devices also utilized an embedded Cu heat-sink layer (~ μm's thick) to reduce thermal gradients within the array and cross-talk between pixels[40]. In order to limit the loss of energetic phonons directly to the substrate, created during the thermalization process, the absorber stem contact region has been reduced significantly to a series of 5 dots, compared to the standard T-stem geometry used for membrane isolated devices[38].
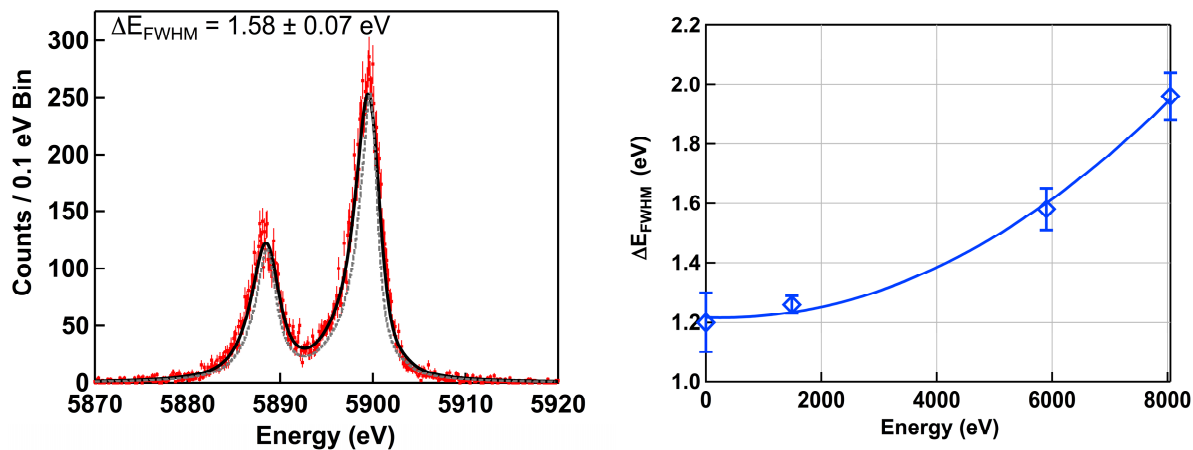

Figure 10. Measured spectrum (left) corresponding to Mn-Kα for a small pixel TES originally developed for solar astronomy[38], the solid line is the best fit to data and the dashed line is natural line shape of the complex from Hölzer et al. (1997)[33]. Also shown (right) is the ΔE_{FWHM} as a function of energy for the same device (spectral measurements were taken at Al-Kα (1.5 keV), Mn-Kα (5.9 keV) and Cu-Kα (8 keV)). The blue line is a polynomial fit to the data.

The miniaturization of Mo/Au TES to lateral size scales of ~ 10's μm has significant impact on transition properties and the operating temperature. Over these size scales the intrinsic transition temperature of the Mo/Au layer T_{Ci} is enhanced by the proximitization from the higher T_C (~ 9 K) Nb leads[31]. This effect is highly dependent on the current running through the sensor. Similarly the addition of normal metal Au stripes proximitizes the surrounding area and significantly suppresses the effective transition temperature[30]. These two competing effects means that the effective under-bias operating temperature of the device, T_0, is highly dependent on geometry and the bias current flowing through it. For these devices $T_{\text{Ci}} \sim 135$ mK but $T_0 = 90$ mK. For the much larger 140 μm LPA pixels the difference between the T_{Ci} and T_0 is only ~ 5 mK. Although the SPA α values are generally similar to that of the LPA, the β values are an order of magnitude higher. This is not fully understood, however it is thought to be associated with the lateral proximity effect dominating the transition physics over these reduced size scales[32]. The high β impacts performance by increasing the near-equilibrium Johnson noise thus degrading resolution. However, this is in part compensated for by the much-reduced

heat capacity. The high β also acts to suppress changes in resistance and therefore improves linearity for a device that would otherwise have limited dynamic range because of the very low heat capacity. Note that for the SPA design parameters listed in Table 1. we include a non-zero unexplained noise factor ($M^2 \sim 0.8$). This may be related to the slightly higher α values for these pixels.

Since the total heat capacity and the thermal decay time are functions of T_0, by designing the devices for different operating temperature, different performance optimizations have been achieved. The devices with the very highest T_0 measured to date had $T_0 \approx 160$ mK and the response to X-ray events in the transition had a decay time of approximately 25 μs. While an energy resolution of $\Delta E_{FWHM} = 2.2$ eV at Mn-Kα was achieved in such a pixel, and it would be the most ideal for accommodating ~ 1000 cps, the speed of this pixel type is not considered an option due to the inability to read out such a device while multiplexing. Similar devices with absorber dimensions 65 μm $\times$ 65 μm $\times$ 5 μm of Au, operating at $T_0 \approx 80$ mK, achieved $\Delta E_{FWHM} = 0.9$ eV at Al-Kα[41]. Pixels with dimensions 45 μm $\times$ 45 μm $\times$ 4.2 μm and operating even lower at $T_0 \approx 55$ mK (whilst running the heat bath at $T_b = 37$ mK) demonstrated $\Delta E_{FWHM} = 0.7$ eV at Al-Kα[42]. The pulse decay time was ~ 1.2 ms. Because of the small C and G_b these pixels have reduced dynamic range and slower decays times but have excellent resolving power at 1.5 keV. We are currently studying whether such optimizations could be implemented for the X-IFU specifically targeted at the energy resolution goal of 1.5 eV (assuming the use of defocusing to achieve the count-rate goal). To achieve an instrument resolution of 1.5 eV an underlying detector resolution of < 1 eV would likely be required. This could be achieved with pixels on a finer pitch (to reduce C). However with the proposed SPA pitch this is challenging and would require both a reduced operating temperature $T_0 < 65$ mK coupled with ~ 50 % the proposed thickness of Au. A significantly thicker Bi layer would need to be used if the same QE were required. The diffusivity properties of thick Bi would need to be verified at these lower operating temperatures.

3.4 Hybrid array implementation

The detector technologies discussed in the previous section have been demonstrated on wafers that use uniform bilayer and absorber depositions. However the use of a hybrid array assumes the ability to independently optimize different regions of a single fabricated wafer for different desired pixel properties. Thus new processing techniques are being developed to enable hybrid arrays. Some of the technical challenges are listed below.

- Absorber composition. Different LPA+SPA configurations will likely require different absorber composition to simultaneously achieve the required C and QE on both pixel types. We have recently demonstrated the ability to deposit different absorber depositions in prototype hybrid arrays. Figure 11 shows a test array where only the absorbers were deposited to test fabrication processing. We have deposited up to ~ 4 μm thick Au absorbers surrounded by an array of larger 250 μm pitch pixels using composite Bi(3 μm)/Au(2.5 μm) absorbers. After an initial 2.5 μm Au deposition everywhere, the different regions are masked in turn to allow deposition of the additional Au or Bi layers in the appropriate regions. The gaps between the absorbers are defined by ion-beam milling. The etch rate of Bi and Au are significantly different, thus we are now developing the processing techniques to produce uniform (~ 4 μm) gaps between pixels over both absorber types. We have recently demonstrated 4 μm gaps are achievable for the test deposition layers discussed above and are now working to achieve similar gaps for thicker Bi deposition layers closer to the 4 μm LPA target.

- Transition temperature. The under bias operating temperature of the TES T_0 depends on the Mo/Au thickness as well as the geometric details of the device. The proposed LPA and SPA pixels have the same assumed T_0. However, because of their different geometries this assumes different Mo/Au deposition thickness and intrinsic transition temperatures T_{Ci}. Thus we are studying techniques to achieve different Mo/Au bilayer thicknesses in different parts of the array to tune the T_0 independently. This could be achieved either by depositing different Mo/Au thicknesses or by depositing uniform Mo/Au and ion-beam milling to remove some of the Au in one region. In addition we are examining different geometric optimizations (TES size, normal metal stripe density and geometry) that may allow tunability in T_0 with the same TES bilayer deposition. On a recent prototype hybrid array we achieved approximately 20 mK difference in T_0 for the small pixels (90 mK) compared with the standard pixels (70 mK) with the same Mo/Au thickness but different normal metal features.

- Heat-sinking. The process needed to heat-sink the SPA is very different to that of the LPA pixels, and the two types of heat-sinking need to be integrated. The heat-sinking of pixels is important first to avoid heat bath temperature gradients within an array caused by the bias power of all pixels, and second, to reduce thermal

cross-talk between pixels. If the heat-sinking is not sufficient the bias power of all the pixels can potentially increase the bath temperature of pixels towards the center of the array, affecting the uniformity of performance. The thermal conductance of the silicon muntins is not sufficient in arrays of the size scale needed for the X-IFU. Therefore, the back-side of the muntins are coated with a layer of high thermal conductivity Cu (> 2μm thick). The heat sink layers embedded into the Si substrate that have been used on solar arrays cannot readily be integrated into to SPA in a hybrid configuration. We are examining an approach whereby the central SPA is deposited on a single large membrane. Heat sinking can then be achieved by depositing ~ μm thick Cu layer over the whole membrane. The LPA can be heat sunk in the usual way. A schematic of this concept is shown in Fig. 12.

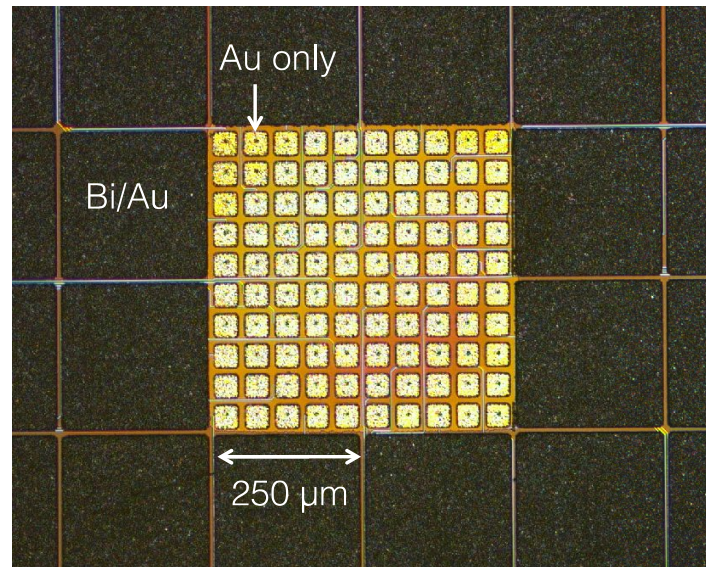
Figure 11. SEM image of a prototype hybrid array consisting of a 10×10 array of 50 μm pixels with thick Au absorbers surrounded by an array of larger 250 μm pitch pixels using composite Bi/Au absorbers. These fabrication demonstration arrays include just the absorber layers with no TESs.
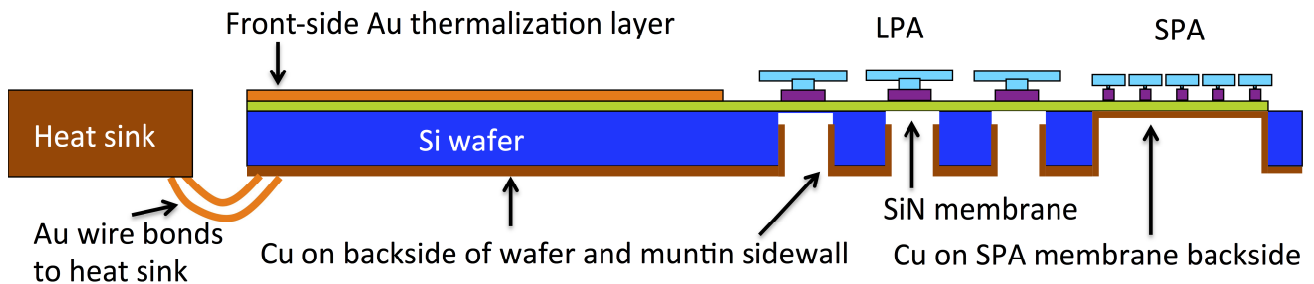

Figure 12. Cartoon cross-section of hybrid array concept (not to scale) showing heat-sinking approach under study. Several μm's of Cu are deposited on the backside of the Si chip and the side-walls between pixels. In order to heat-sink the SPA, Cu is also deposited directly on the back side of the single large membrane.

4. SUMMARY AND CONCLUSIONS

We have presented details of the pixel parameters and array designs under consideration for the Athena X-IFU. These parameters provide a baseline for Phase A studies and are being used for science simulations and further optimization of

the array and FDM readout architecture. The uniform baseline LPA is based around a well-established design. Near-term technology development is targeted at achieving uniform kilo-pixel arrays that are suitable for technology demonstrations with FDM and TDM/CDM. Since the AC pixel characteristics are different to the measured DC characteristics, we are simultaneously studying geometric variations around the reference design in smaller diagnostic chips that could yield improved performance. These designs are drop-in compatible with present the TES design in uniform arrays, thus if design improvements are identified, it can easily be incorporated in to uniform arrays for large-scale multiplexed demonstrations.

Alternatives to the uniform LPA under consideration are targeted at achieving the higher count-rate and/or lower energy resolution goals. These include defocusing the beam and/or implementing a hybrid array. The hybrid array utilizes a reduced-speed LPA coupled with a smaller SPA that can be potentially be optimized to accommodate higher photon fluxes or improved energy resolution at lower count-rates and dynamic range. Initial studies of the beam defocusing suggest the high rate requirement could be accommodated using a reduced speed LPA (as defined in Table 1). If the SPA could be optimized for improved resolution (< 1.5 eV) all instrument goals can be satisfied and the full potential for X-IFU can be realized. However, although the feasibility of these different individual detector optimizations has been demonstrated, integration on to a single detector die is yet to be accomplished. In light of this, the hybrid array technology development is focused around demonstrating the fabrication techniques necessary for optimizing an array for different detector designs.

REFERENCES

[1] Nandra, K., Barret, D., Barcons, X., Fabian, A., den Herder, J.-W., Piro, L., Watson, M., Adami, C., Aird, J., Afonso, J.M., *et al.*, "The Hot and Energetic Universe: A White Paper presenting the science theme motivating the Athena+ mission," ArXiv e-prints (June 2013); and Barcons, X., Nandra, K., Barret, D., den Herder, J.-W., Fabian, A.C., Piro, L., Watson, M. G., and the Athena Team, "Athena: the X-ray observatory to study the hot and energetic universe," J. of Physics Conference Series 610, 012008 (May 2015).

[2] Barret, D., Lam Trong, T., den Herder, J.-W. A., Piro, L., *et al.*, "The Athena X-ray Integral Field Unit," submitted to Proc. SPIE in [Space Telescopes and Instrumentation 2014: Ultraviolet to Gamma Ray], Proceedings of the International Society for Optical Engineering 9905, (2016).

[3] Meidinger, N., Eder, J., Eraerds, T., Nandra, K., Pietschner, D., Plattner, M., Rau, A., Strecker, R., "The wide field imager instrument for Athena," in [Space Telescopes and Instrumentation 2014: Ultraviolet to Gamma Ray], Proceedings of the International Society for Optical Engineering (SPIE) 9905, 990529 (2016). doi:10.1117/12.2231604.

[4] Irwin, K.D. and Hilton, G.C., "Transition-edge sensors," in [Cryogenic Particle Detection], ed, Enss, C., 63-149, Springer, Berlin, Heidelberg (2005).

[5] den Hartog, R., Beyer, J., Boersma, D., Bruijn, M., Gottardi, L., Hoevers, H., Hou, R., Kiviranta, M., de Korte, P., van der Kuur, J., van Leeuwen, B.-J., Lindeman, M., Nieuwenhuizen, A.,"Frequency domain multiplexed readout of TES detector arrays with baseband feedback," IEEE Trans. Appl. Supercond. 21, 289-293 (2011).

[6] Jackson, B., van Weers, H., van der Kuur, J., *et al.*, "The focal plane assembly for the Athena X-ray Integral Field Unit instrument," SPIE 2016, in [Space Telescopes and Instrumentation 2014: Ultraviolet to Gamma Ray], Proceedings of the International Society for Optical Engineering (SPIE) 9905 (2016).

[7] Brand, T., Dauser. T., Wilms J., "Athena X-IFU response files," document ECAP-XIFU-RSP-005, April 2016.

[8] den Hartog, R., Barret, D., Gottardi, L., den Herder, J.-W., Jackson, B., de Korte, P., van der Kuur, J.,van Leeuwen, B.-J., van Loon, D., Nieuwenhuizen, A., and Ravera, L., "Requirements for the detectors and read-out of ATHENA X-IFU," in [Space Telescopes and Instrumentation 2014: Ultraviolet to Gamma Ray], Proceedings of the International Society for Optical Engineering (SPIE) 9144 , 91445Q (2014).

[9] van der Kuur, J., Gottardi, L., Akamatsu, H., *et al.*, "Optimizing the multiplex factor of the frequency domain multiplexed readout of the TES-based microcalorimeter imaging array for the X-IFU instrument on the ATHENA x-ray observatory," in [Space Telescopes and Instrumentation 2014: Ultraviolet to Gamma Ray], Proceedings of the International Society for Optical Engineering (SPIE) 9905 (2016).

[10] Doriese, W.B., Adams, J.S., Hilton G.C., Irwin, K.D., Kilbourne, C.A., Schima, F.J., Ullom, J.N., "Optimal filtering, record length, and count rate in transition-edge-sensor microcalorimeters," AIP Conf. Proc. 1185, 450 (2009).

[11] Peille, P., Ceballos, M.T., Cobo, B., *et al.*, "Performance assessment of different pulse reconstruction algorithms for the Athena X-ray Integral Field Unit," in [Space Telescopes and Instrumentation 2014: Ultraviolet to Gamma Ray], Proceedings of the International Society for Optical Engineering (SPIE) 9905, 99055L (2016). doi:10.1117/12.2232011.

[12] Peille, P., Wilms, J., Brand, T., *et al.*, "The X-IFU end-to-end simulations performed for the TES array optimization exercise," in [Exploring the Hot and Energetic Universe: The first scientific conference dedicated to the Athena X-ray observatory], Madrid, Spain (8-10 September 2015).

[13] van der Kuur, J., Beyer, J., Bruijn, M., *et al.*, "The SPICA-SAFARI TES Bolometer Readout: Developments Towards a Flight System," J. Low Temp. Phys. 167, 561-567 (2012).

[14] Gottardi, L., Kiviranta M., van der Kuur, J., Akamatsu, H., Bruijn, M.P., den Hartog, R., "Nearly quantum limited two-stage squid amplifiers for the frequency domain multiplexing of tes based x-ray and infrared detectors," IEEE Trans on Appl. Superc. 25, 1-4 (2015).

[15] Doriese, W.B., Morgan, K.M., Bennett, D.A., Denison, E.V., Fitzgerald, C.P., Fowler, J.W., Gard, J.D., Hays-Wehle, J.P., Hilton, G.C., Irwin, K.D., Joe, Y.I., Mates, J.A.B., O'Neil, G.C., Reintsema, C.D., Robbins, N.O., Schmidt, D.R., Swetz, D.S., Tatsuno, H., Vale, L.R., Ullom, J.N., "Developments in Time-Division Multiplexing of X-ray Transition-Edge Sensors," J. Low Temp. Phys 184, 389-395 (2016).

[16] Irwin, K.D., Cho, H.M., Doriese, W.B., *et al.*, "Advanced code-division multiplexers for superconducting detector arrays," J. Low Temp. Phys. 167, 588-594 (2012).

[17] Bruijn, M. Gottardi, L. den Hartog, R., *et al.*, "Tailoring the high-q lc filter arrays for readout of kilo-pixel tes arrays in the spica-safari instrument," J. Low Temp. Phys. 176, 421-425 (2014).

[18] Akamatsu, H., Gottardi, L., van der Kuur, J., *et al.*, "Development of the frequency domain multiplexing for the x-ray integral field unit (X-IFU) on the ATHENA," in [Space Telescopes and Instrumentation 2014: Ultraviolet to Gamma Ray], Proceedings of the International Society for Optical Engineering (SPIE) 9905 (2016).

[19] Iyomoto, N., Kilbourne, C.A., Bandler, S.R., Brekosky, R.P., Brown, A.-D., Chervenak, J.A., Finkbeiner, F.M., Kelley, R.L., Porter, F.S., Smith, S. J., Sadleir, J.E., Figueroa-Feliciano, E., "Close-packed arrays of transition-edge x-ray microcalorimeters with high spectral resolution at 5.9 keV," Appl. Phys. Lett. 92, 013508 (2008).

[20] Kilbourne, C.A., Bandler, S.R., Brown, A.-D., Chervenak, J.A., Figueroa-Feliciano, E., Finkbeiner, F.M., Iyomoto, N., Kelley, R.L., Porter, F.S., Smith, S.J., "Uniform high spectral resolution demonstrated in arrays of TES x-ray microcalorimeters," in [UV, X-Ray, and Gamma-Ray Space Instrumentation for Astronomy XV], ed. O.H.W. Siegmund, Proceedings of the Society of Photo-Optical Instrumentation Engineers (SPIE) 6686, 668606 (2007).

[21] Kelley, R.L., Bandler, S.R., Doriese, W.B., Ezoe, Y., Fujimoto, R., Luciano, G., Den Hartog, R., Den Herder, J.-W., Hoevers, H., Irwin, K.D., Ishisaki, Y., Kilbourne, C.A., De Korte, P., Van Der Kuur, J., Mitsuda, K., Ohashi, T., Piro, L., Porter, F.S., Sato, K., Shinozaki, K., Shirron, P., Smith, S.J., Takei, Y., Whitehouse, P., Yamasaki, N.Y., "The X-Ray Microcalorimeter Spectrometer for the International X-Ray Observatory," AIP conference Proc. 1185, 757-760 (2009).

[22] Kilbourne, C.A., Doriese, W.B., Bandler, S.R., Brekosky, R.P., Brown, A.-D., Chervenak, J.A., Eckart, M.E., Finkbeiner, F.M., Hilton, G.C., Irwin, K.D., Iyomoto, N., Kelley, R.L., Porter, F.S., Reintsema, C.D., Smith, S.J., Ullom, J.N., "Multiplexed readout of uniform arrays of TES x-ray microcalorimeters suitable for Constellation-X," in [Space Telescopes and Instrumentation 2008: Ultraviolet to Gamma Ray], ed. M.J.L. Turner and K.A. Flanagan, proceedings of the Society of Photo-Optical Instrumentation Engineers (SPIE) 7011, 701104, (2008).

[23] Eckart, M.E., Adams, J.S., Bailey, C.N., Bandler, S.R., Busch, S.E., Chervenak, J.A., Finkbeiner, F.M., Kelley, R.L., Kilbourne, C.A., Porter, F.S., Sadleir, J.E., Smith, S.J., "Kilopixel X-ray Microcalorimeter Arrays for Astrophysics: Device Performance and Uniformity," J. Low Temp. Phys 167, 732-740 (2012).

[24] Smith, S.J., Adams, J.S., Bandler, S.R., Busch, S.E., Chervenak, J.A., Eckart, M.E., Finkbeiner, F.M., Porter, F.S., Kilbourne, C.A., Kelley, R.L., Lee, S.-J., Porst, J.-P., Porter, F.S., Sadleir, J.E., "Characterization of Mo/Au transition-edge sensors with different geometric configurations," J. Low Temp. Phys. 176, 356-362 (2014).

[25] Smith, S.J., Adams, J.S., Bandler, S.R., *et al.*, "Uniformity of Kilo-Pixel Arrays of Transition-Edge Sensors for X-ray Astronomy," IEEE Trans. Appl. Supercon., 25, 2100505 (2015).

[26] Brown, A.-D., Bandler, S.R., Chervenak, J.A., Figueroa-Feliciano, E., Finkbeiner, F., Iyomoto, N., Kelley, R.L., Kilbourne, C.A., Porter, F.S., Saab, T., Sadleir, J., Smith, S.J., "Absorber Materials for Transition-Edge Sensor X-ray Microcalorimeters," J. Low Temp. Phys. 151, 413-417 (2008).

[27] Collan, H.K., Krusius, M., Pickett, G.R., "Specific Heat of Antimony and Bismuth between 0.03 and 0.8 K," Phys. Rev. B 1, 2888 (1970).

[28] Eckart, M.E., Adams, J.S., Bandler, S.R., Brekosky, R.P., Brown, A.-D., Chervenak, J.A., Finkbeiner, F.M., Kelley R.L., Kilbourne, C.A., Porter, F.S., Sadleir, J.E., Smith, S.J., "Experimental Results and Modeling of Low-Heat-Capacity TES Microcalorimeters for Soft-X-ray Spectroscopy," AIP conference Proc. 1185, 430-433 (2009).

[29] Hoevers, H.F.C., Ridder, M.L., Germeau, A., Bruijn, M.P., de Korte, P.A.J., Wiegerink, R.J., "Radiative ballistic phonon transport in silicon-nitride membranes at low temperatures," Appl. Phys. Lett. 86, 251903, 2005.

[30] Sadleir, J.E., Smith, S.J., Robinson, I.K., Finkbeiner, F.M., Chervenak, J.A., Bandler, S.R., Eckart, M.E., Kilbourne, C.A., "Proximity Effects and Non-equilibrium Superconductivity in Transition-Edge Sensors," Phys. Rev. B 84, 184502 (2011).

[31] Sadleir, J.E., Smith, S.J., Bandler, S.R., Chervenak, J.A., Clem, J.R., "Longitudinal proximity effect in superconducting transition-edge sensors," Phys. Rev. Lett. 104, 047003 (2010).

[32] Ullom, J.N., Bennett, D.A., "Review of superconducting transition-edge sensors for x-ray and gamma-ray spectroscopy," Supercond. Sci. Technol. 28, 084003 (2015).

[33] Holzer, G., Fritsch, M., Deutsch, M., Hartwig, J., Forster, E., "Kα1,2 and Kβ1,3 x-ray emission lines of the 3d transition metals," Phys. Rev. A 56, 4554–4568 (1997).

[34] Bearden J.A., "X-Ray Wavelengths," Rev. Mod. Phys. 39, 78 (1967).

[35] Krause, M.O., Oliver, J.H., "Natural widths of atomic K and L levels, Kα X-ray lines and several K L L Auger lines," J. Phys. Chem. Ref. Data 8, 329 (1979).

[36] Smith, S.J., Adams, J.S., Bailey, C.N., Bandler, S.R., Busch, S.E., Chervenak, J.A., Eckart, M.E., Finkbeiner, F.M., Kilbourne, C.A., Kelley, R.L., Lee, S.-J., Porst, J.-P., Porter, F.S., Sadleir, J.E., "Implications of weak-link behavior on the performance of Mo/Au bilayer transition-edge sensors," J. App. Phys. 114, 074513 (2013).

[37] Akamatsu, H., Gottardi, L., Adams, J. *et al.*, "Single Pixel Characterization of X-Ray TES Microcalorimeter Under AC Bias at MHz Frequencies," IEEE Trans. on Appl Supercon. 23, 2100503 (2013).

[38] Smith, S.J., Adams, J.S., Bailey, C.N., Bandler, S.R., Chervenak, J.A., Eckart, M.E., Finkbeiner, F.M., Kelley, R.L., Kilbourne, C.A., Porter, F.S., Sadleir, J.E., "Small Pitch Transition-Edge Sensors with Broadband High Spectral Resolution for Solar Physics," J. Low Temp. Phys. 167, 168-175 (2012).

[39] Lee, S.J., Bandler, S.R., Busch, S.E. *et al.*, "High Count-Rate Studies of Small-Pitch Transition-Edge Sensor X-ray Microcalorimeters," J Low Temp. Phys. 176, 597 (2014).

[40] Finkbeiner, F.M., Bailey, C.N., Bandler, S.R., Brekosky, R.P., Brown, A.-D., Chervenak, J.A., Eckart, M.E., Kelley, R.L., Kelly, D.P., Kilbourne, C.A., Porter, F.S., Sadleir, J.E., Smith, S.J., "Development of Superconducting Silicon Dioxide Embedded Heatsinking Layers for Compact Arrays of X-ray TES Microcalorimeters," IEEE Trans. Appl. Supercon. 21, 223-226 (2011).

[41] Bandler, S.R., Adam, J.S., Bailey C.N., *et al.*, "Advances in Small Pixel TES-Based X-Ray Microcalorimeter Arrays for Solar Physics and Astrophysics," IEEE Trans on Appl. Supercon., 23, 2100705 (2013).

[42] Lee, S.J., Adams, J.S., Bandler, S.R., Chervenak, J.A., Eckart, M.E., Finkbeiner, F.M., Kelley, R.L., Kilbourne, C.A., Porter, F.S., Sadleir, J.E., Smith, S.J., Wassell, E.J., "Fine pitch transition-edge sensor X-ray microcalorimeters with sub-eV energy resolution at 1.5 keV," Appl. Phys. Lett. 107, 223503 (2015).